Renewable Energy 263 (2026) 125528

Contents lists available at ScienceDirect

Renewable Energy

journal homepage: www.elsevier.com/locate/renene

Efficiency optimization of power-to-ammonia systems based on pressurized solid oxide electrolysis

Daruska Miric-Fuentes [a], Matthias Riegraf [a,*], Faisal Sedeqi [a], Srikanth Santhanam [b], Marc P. Heddrich [a], S. Asif Ansar [a]

[a] German Aerospace Center (DLR), Institute of Engineering Thermodynamics, 70569, Stuttgart, Germany
[b] Shell Global Solutions International B.V., 1030 BN, Amsterdam, Netherlands

ARTICLE INFO

Keywords:
Steam electrolysis
SOEL
SOEC
Haber-bosch process
Pressurized SOEC

ABSTRACT

Solid oxide electrolysis cells (SOECs) enable efficient hydrogen production by utilizing waste heat for steam evaporation, providing strong synergies with exothermic ammonia synthesis. However, there is a need for efficient systems designs to couple these processes for renewable ammonia production. Here, the influence of operating pressure and system configuration on power-to-ammonia (PtA) efficiency is investigated using an experimentally validated model of electrolyte-supported cell (ESC)-based stacks. Main findings were: (1) PtA efficiencies increase with SOEC pressurization in systems without sweep air, reaching 72% at 8 bar, while sweep air systems peak at ~69% at 2 bar due to air compression demand at elevated pressures. (2) Part-load operation in modular plants reduces efficiency, dropping to 45% at 10% load because of module hot standby consumption. (3) Waste heat from the Haber–Bosch process combined with SOEC off-gas recovery, meets steam demand in most cases, with up to 62% supplied by the SOEC itself. (4) At high pressure without sweep air, electrical steam generation is required due to reduced off-gas heat and higher boiling points. In such a case, increasing the recirculation ratio can increase system efficiency by reducing evaporator load.

1. Introduction

Ammonia is the second most-produced chemical globally, with an annual capacity of approximately 180 million tons, accounting for nearly 2% of total global energy consumption. While its primarily used as fertilizer, ammonia is also a feedstock for basic chemicals and a potential maritime fuel [1]. The Haber-Bosch (HB) process has dominated ammonia production for over a century, resulting in highly efficient, capital-intensive plants that benefit from economies of scale [2], operate continuously and typically include a cryogenic air separation unit (ASU) for nitrogen production, a methane steam reforming (SMR) unit for hydrogen generation, and the HB synthesis loop. The core reaction follows:

$$3H_2 + N_2 \rightarrow 2NH_3, \Delta_r H_{450\,^\circ C} = -105.9\ kJ/mol \quad (1)$$

Despite its efficiency, conventional ammonia synthesis remains energy-intensive and dependent on fossil-fuel-derived hydrogen, generating significant CO_2 emissions. Integrating electrolytic green hydrogen production presents a pathway toward sustainable ammonia production. Among the electrolysis technologies, solid oxide electrolysis cells (SOECs) offer by far the highest energy efficiency, especially when excess heat is available for steam generation, making them well-suited for integration with exothermic chemical processes such as ammonia synthesis.

Progress in SOEC technology has led to rapid scaling in recent years, with manufacturing capacities approaching gigawatt (GW) levels [3], and large-scale megawatt (MW) demonstration plants being installed [4].

Most SOEC demonstration plants operate at ambient pressure, but pressurized operation could reduce capital expenditure (CAPEX) by potentially eliminating compression stages and reducing the required heat exchanger area [5]. Pressurized steam electrolysis can also increase system efficiency by allowing water compression instead of gaseous hydrogen [6,7]. However, integration of SOECs into pressure vessels is often necessary to prevent high differential pressures, and the energy savings on the fuel side may be offset by the compression of large air flow rates which are required to maintain safe oxygen partial pressures [8,9]. Thus, optimized stacks operated without sweep air are

* Corresponding author.
E-mail address: Matthias.riegraf@dlr.de (M. Riegraf).

https://doi.org/10.1016/j.renene.2026.125528
Received 23 October 2025; Received in revised form 13 January 2026; Accepted 1 March 2026
Available online 3 March 2026

increasingly of interest.

System-level constraints include fuel gas recirculation to maintain Ni/cermet electrodes in a reduced state, implemented as high-temperature recirculation (HTR) directly after the outlet, intermediate-temperature recirculation (ITR) after the recuperator, or low-temperature recirculation (LTR) after the condenser. HTR/ITR can increase global reactant conversion (RC) but add cost [10], while LTR is simpler and less costly but leads to lower global RC.

Optimal recirculation strategies depend on single-pass RC. High recycle ratios (RRs) via HTR/ITR are most beneficial at low single-pass RC [11], but increase the Nernst potential due to higher reactant concentrations, reducing performance. Generally, further research is required to develop optimized fuel gas recirculation strategies that increase system efficiency.

A key challenge in integrating SOECs with ammonia synthesis is the heat balance. The ammonia heat (~31 kJ/mol$_{H2}$) is insufficient to fully meet steam generation heat demand (−40.7 kJ/mol$_{H2O}$). Combination of heat from the HB reactor, intercoolers between compression stages and SOEC off-gases could fully cover the steam evaporation energy demand in some system configurations, whereas in other configurations, for instance, at elevated operating pressure of 30 bar, electric heaters would still be needed to cover the remaining heat of evaporation [12, 13].

So far, steady-state SOEC operation has been preferred, but fluctuating electricity prices due to intermittently available renewable energy sources (RES) may necessitate dynamic operation [14]. As a result, the entire process chain must be designed to ensure the continuous availability of process heat for SOEC steam generation, which may require advanced heat management.

Previous *Renewable Energy* publications highlight the energetic [15] and economic SOEC advantages [16] in PtA, and focused on SOEC coupling strategies with upstream solar thermal plants [17]. Here, we focus on technical coupling strategies of SOEC with downstream ammonia synthesis including heat integration. Using an experimentally validated stack model of state-of-the-art electrolyte-supported cell (ESC) technology, the study examines the impact of temperature, pressure, recirculation strategies, sweep air and part-load operation on global RC and system efficiency.

2. Power-to-Ammonia systems

2.1. Systems description

In this modeling study, the baseline PtA system comprised hydrogen and nitrogen production section coupled to a HB loop for ammonia synthesis. Partial thermal integration was implemented to subsequently find optimal heat integration possibilities between sections.

Feed water was conditioned and supplied to a SOEC reactor. The resulting stream, consisting of hydrogen and residual water, was split: one fraction was recycled to the SOEC, while the other was dried and sent downstream. Simultaneously, nitrogen produced in an ASU was conditioned and mixed with the purified hydrogen to form synthesis gas. This mixture entered the HB loop, where it was compressed and reacted in three adiabatic reactors arranged in series. The reactor effluent was

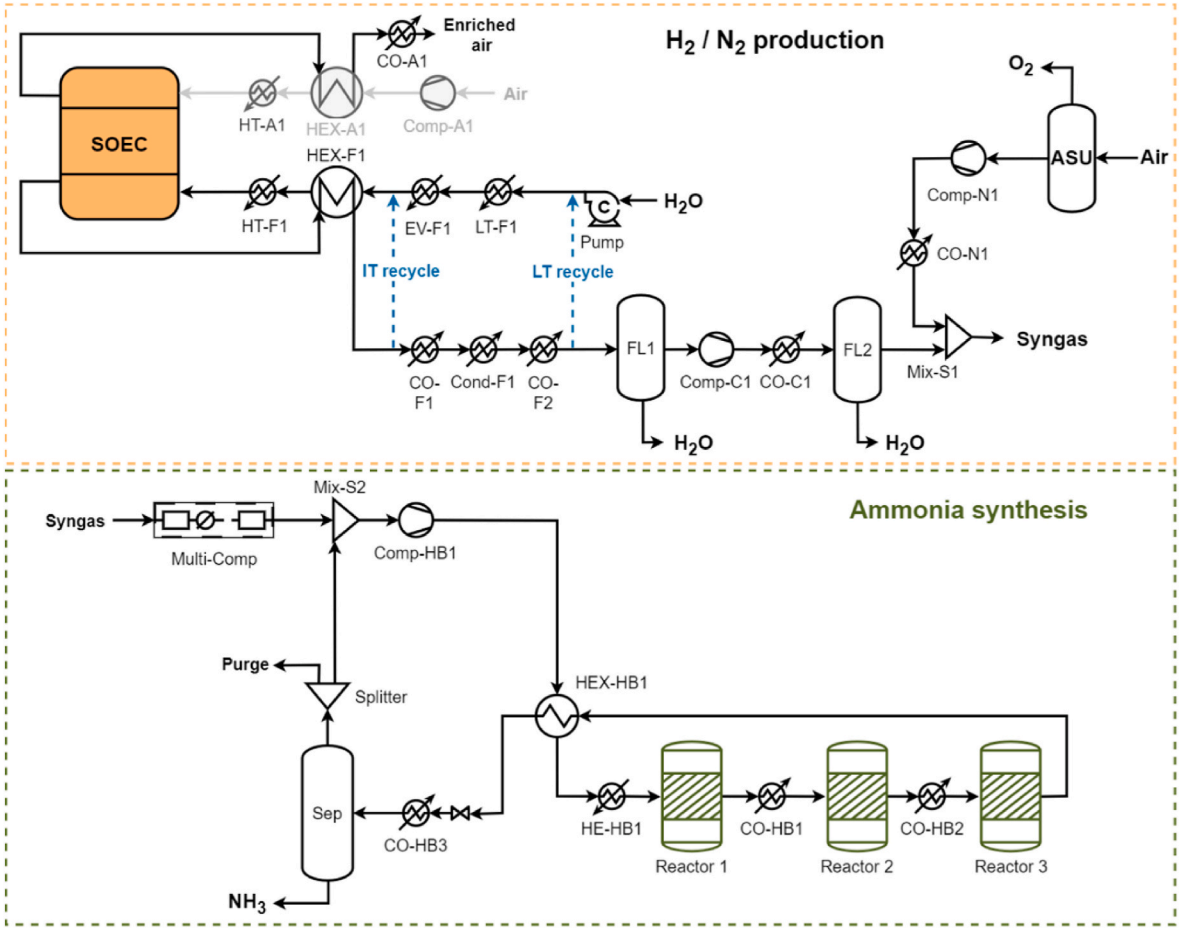

Fig. 1. PtA process flow diagram divided into the SOEC and the ammonia sections. The SOEC section shows the three configurations analyzed: (i) SOEC with internal LTR (LT dashed blue), (ii) SOEC with internal ITR (IT dashed blue), both using sweep air (gray components), and (iii) a no sweep air case with internal recycling at the ITR point. (For interpretation of the references to colour in this figure legend, the reader is referred to the Web version of this article.)

cooled to separate ammonia, while unreacted synthesis gas was partially recycled to enhance overall conversion, with the remaining fraction purged.

To evaluate optimized PtA configurations with respect to thermal integration and efficiency, three SOEC process layouts were analyzed. These configurations investigated the impact of different recirculation strategies and the use or omission of sweep air, as depicted in Fig. 1. The first system employed an LTR after the condenser, recycling hydrogen and condensed water to the evaporator, and using sweep air stream. The second layout featured an ITR, with sweep air, while the third operated with an ITR but with no sweep air (or NSA + ITR).

2.2. Process unit models

The components and systems were modelled using the in-house simulation software CELESTE presented in Ref. [9]. Feed streams entered the system at ambient conditions (25 °C, 1 bar). The detailed descriptions of model assumptions and operating conditions for both system sections are provided below.

2.2.1. Hydrogen and nitrogen synthesis

Liquid feed water was pressurized to the SOEC operating pressure using an isentropic pump with an efficiency of 85%, heated in the LT-F1 electric heater, and subsequently evaporated in EV-F1. The evaporation heat demand was initially treated as electrical heating demand; however, its partial or full coverage via waste heat recovery from the SOEC and HB sections was later assessed for each configuration. For configurations employing sweep air, the feed air stream was compressed in an isentropic compressor (Comp-A1) with 70% efficiency. Heat recuperation from the SOEC outlet gases was achieved using two heat exchangers (HEX-F1 for the fuel side and HEX-A1 for the air side, respectively), modelled via the number of transfer unit (NTU) method with an effectiveness of 0.8 and negligible heat losses. Electrical heaters (HT-F1 and HT-A1) then adjusted fuel and air temperatures to meet the SOEC operating requirements under all conditions.

The SOEC was modelled using the experimentally validated 0D model from Ref. [9], assuming isothermal operation at 800 °C and no heat losses. The SOEC operating pressure was varied between 1 and 8 bar. The single-pass RC, defined in Eq. (2), was fixed at 70%, and the outlet oxygen molar fraction in the air stream was set to 40%.

$$RC = \frac{-I\,N_{cells}}{2\,F\,\dot{n}'_{H_2O,SOEC}} \times 100 \tag{2}$$

Here, F is the Faraday's constant, I the SOEC current, N the number of cells, and $\dot{n}'_{H_2O}$ the inlet steam molar flow rate. To ensure a minimum hydrogen concentration of 10% at the SOEC inlet for Ni/cermet electrode stability, either an LTR or an ITR stream was employed. The LTR operated at 25 °C, while the ITR temperature varied with SOEC operating pressure, from 265 to 318 °C between 1 and 8 bar. The parameters varied during the simulations included the molar flow rates of feed water and sweep air (when applicable), as well as the SOEC current. The global RC (RC_{global}), defined in Eq. (3) as the ratio of reacted water to total SOEC feed water, was also calculated.

$$RC_{global} = \frac{\dot{n}'_{H_2O,Pump} - \dot{n}'_{H_2O,FL1}}{\dot{n}'_{H_2O,Pump}} \times 100 \tag{3}$$

The hydrogen-steam outlet mixture was cooled and partially condensed before separation. Several technologies can achieve high-purity hydrogen separation, including pressure swing adsorption, temperature swing adsorption, membranes, and cryogenic separation [18]. Because detailed modeling these processes lies beyond the scope of this conceptual study, a simplified approach using two flash separator stages with intermediate compression and cooling was adopted, offering a more straightforward and computationally efficient solution. In the first flash (FL1), more than 92% of the water was removed, depending on SOEC operating pressure. In the second stage, the stream was compressed to 10 bar (Comp-C1), cooled to 25 °C (CO-C1), and sent to a second flash (FL2), reducing residual steam below 5 ppm to avoid catalyst poisoning in the HB reactors [19].

The ASU was modelled as a cryogenic distillation process with a specific energy consumption of 108 kWh/t_{N2} [20]. The inlet air composition was assumed to be 21% O_2 and 79% N_2, producing pure nitrogen at 8 bar. The ASU feed flow rate was adjusted to maintain the stoichiometric H_2/N_2 ratio of 3:1 required for ammonia synthesis.

2.2.2. Ammonia synthesis

The synthesis gas entered the ammonia section at 10 bar, significantly below typical HB operating pressures (150-250 bar). Compression to 194 bar was achieved using a two-stage compressor (Multi-Comp) with 89% isentropic efficiency and internal cooling, maintaining a constant outlet temperature of 201.7 °C, consistent with centrifugal compressors limits [21]. Intercooler outlet temperatures were fixed at 25 °C. An additional isentropic compressor (Comp-HB1, 70% efficiency) compensated for loop pressure losses, resulting in a final pressure of 205 bar at the inlet of the first HB reactor.

The pressurized synthesis gas was preheated in a heat exchanger (HEX-HB1, effectiveness 0.8) using waste heat from the final reactor effluent, followed by an electrical heater (HE-HB1) to reach the required inlet temperature in the first reactor. Ammonia synthesis was modelled using three adiabatic, kinetic-based reactors in series with intermediate cooling, achieving a typical per pass conversion of 35% [22]. Reaction kinetics followed the industrial reactor model proposed in Ref. [23] and are described by Eqs. (4)–(6).

$$r_{NH_3} = 2f\left(k_1\frac{p_{N_2}p_{H_2}^{1.5}}{p_{NH_3}} - k_{-1}\frac{p_{NH_3}}{p_{H_2}^{1.5}}\right) \tag{4}$$

$$k_1 = 1.79 \times 10^4\ exp\left(-\frac{87090}{RT}\right) \tag{5}$$

$$k_{-1} = 2.57 \times 10^{16}\ exp\left(-\frac{198464}{RT}\right) \tag{6}$$

Where f is a correction factor set to 4.75, k_1 and k_{-1} are the forward and reverse pre-exponential factors, p denotes partial pressure, R is the universal gas constant, and T the outlet temperature. Reactor inlet temperatures were set to 410 °C for the first bed and 420 °C for the subsequent two beds, with a pressure drop of 1 bar per reactor.

After reaction and heat recovery, the product stream was cooled and sent to a separation unit, where liquid ammonia was removed. The overhead gas, containing approximately 5% ammonia, was mostly recycled (98%) to the reactor loop to enhance overall conversion, while the remaining 2% was purged.

2.3. Key performance indicators

System performance was evaluated using the following key performance indicators (KPI). The lower heating value (LHV) efficiency was defined as,

$$\eta_{sys} = \frac{\dot{m}_{NH_3}\,LHV_{NH_3}}{\dot{W}_{in} + \dot{Q}_{in}} \times 100 \tag{7}$$

Where $\dot{m}_{NH_3}$ is the produced ammonia mass flow rate, LHV_{NH_3} the LHV of ammonia, $\dot{W}_{in}$ the total power demand of compressors, pump, electrolyzer and ASU, and $\dot{Q}_{in}$ the total electrical heating demand (e.g. gas preheating before the SOEC). For the ideal case in which the total heat demand ($\dot{Q}_{in}$) was fully supplied via heat integration (HI), the LHV efficiency with perfect high-grade heat availability (PHA) was defined as:

$$\eta_{sys,PHA} = \frac{\dot{m}_{NH_3} LHV_{NH_3}}{\dot{W}_{in}} \times 100 \quad (8)$$

which represents an idealized upper-bound efficiency.

2.4. Assumptions and simplifications

To establish the thermodynamic performance limits of SOEC-based PtA systems, the following idealized assumptions were adopted:

- Isothermal SOEC operation which is typically preferred due to low thermal gradients in the stack.
- No stack module heat losses. Real-life modules were reported to show heat losses of 1.5-3% of full-load power [24,25]. However, larger SOEC modules exhibit lower relative heat losses due to improved surface-to-volume ratios. Hence, we set these heat losses to zero to avoid design-specific constraints, except for the part-load study (below).
- For the study cases with idealized PHA, 100% internal heat recovery, without pinch analysis or heat exchanger network (HEN) design. For more practical considerations, a heat integration study was also conducted (see below).
- Ideal gas behavior, given the high operating temperatures and moderate pressures considered.
- Negligible pressure losses in the SOEC, piping and additional components, to avoid stack and system-specific modeling assumptions.

2.5. Heat integration and part-load operation

Subsequently, to evaluate waste heat recovery potential and minimize external utility demand, a detailed HI analysis was performed. Stream data from all heaters and coolers (temperatures, flow rates, and heat capacities) were extracted from the system simulations presented in Fig. 1 and used to construct composite curves and perform pinch analysis. This yielded an optimized heat exchanger network (HEN) for all process routes. A minimum temperature difference approach (ΔT_{min}) of 10 °C was applied, balancing heat recovery potential with realistic equipment size and cost for shell-and-tube heat exchangers [26]. The analysis was conducted at an SOEC temperature of 800 °C, a single-pass RC of 70%, and an oxygen outlet concentration of 40%, for SOEC pressures of 1, 2 and 8 bar, to assess the impact of pressure on thermal energy reuse and residual cooling demand.

Part-load operation study examined a modular system with ITR and an SOEC operating at 2 bar. Based on the nominal SOEC design, part-load scenarios were simulated by dividing the SOEC nominal power into ten identical modules. Thus, at 60% load, six modules operated under isothermal conditions following the PFD in Fig. 1, while four modules were maintained in hot standby.

In hot standby, each SOEC module operated with a 9:1 water-to-hydrogen inlet ratio and an ITR of 95%. External hydrogen was needed to maintain a 10% inlet hydrogen concentration. The remaining 5% steam-hydrogen mixture was cooled to 25 °C, providing recoverable cooling duty, and routed to flash FL1. Additionally, SOEC heat losses to the environment were included, fixed at 1.5% of the nominal SOEC power, corresponding to a 30 °C temperature difference between inlet and outlet streams. Constant heat losses across the load range were assumed, as stack surface area and SOEC core temperature remain nearly unchanged. A simplified quasi-linear behavior was assumed for all components, including compressors, the HB reactors, and the ASU, across all load operations, with limitations at low-loads neglected. Heat losses from the HB reactors were not considered, except those associated with the off-gas stream. No recirculation blower was modelled, as its electrical consumption has been shown to be negligible in SOEC systems [27]. Finally, a heat integration analysis was performed to both operating and hot-standby modules.

3. Results and discussion

3.1. SOEC and system performance

First, the effect of SOEC operating pressure was numerically assessed for the three system configurations LTR, ITR, and NSA + ITR. Pressure was varied between 1 and 8 bar, while operating conditions of all other components remained constant. An HTR system was initially considered, however, preliminary calculations revealed only marginal differences from ITR, so HTR was treated as equivalent.

Isothermal stack current densities are illustrated in Fig. 2. Increasing pressure reduced current densities due to an increased open circuit voltage (OCV), which in turn decreased the voltage difference between OCV and isothermal voltage. Current densities ranged from 0.37 A/cm^2 at 1 bar to 0.32 A/cm^2 at 8 bar for both LTR and ITR. In the absence of sweep air (NSA + ITR), the current densities showed the same behavior with pressure but were lower, 0.34 A/cm^2 at 1 bar and 0.29 A/cm^2 at 8 bar. These reductions were due to an increased OCV due to pure oxygen on the oxygen side. Operating voltage was 1.29 V at all pressures for the three routes (see supplementary material (SM) Fig. S1), consistent with literature [9]. Nominal operating temperature of 820 °C for the used ESC stack technology is 820 °C where current densities of ~0.5 A/cm^2 can be reached [28]. The operating temperature of 800 °C decreased the current density but could increase stack lifetime. Even higher current densities are generally reached in stacks with fuel electrode-supported cells or ESCs using Sc-stabilized zirconia (ScSZ) electrolytes [29].

System-level results are shown as total specific energy demand (kWh/kg$_{NH3}$) in Fig. 3a. These values showed a similar behavior for LTR and ITR, decreasing from 1 bar to a minimum at 2 bar, then increasing up to 8 bar. Across all pressures, the LTR consistently required more specific energy than the ITR, 9.45 kWh/kg$_{NH3}$ at 1 bar and 9.55 kWh/kg$_{NH3}$ at 8 bar, while ITR ranged from 9.36 to 9.45 kWh/kg$_{NH3}$. In contrast, NSA + ITR decreased continuously from 9.17 kWh/kg$_{NH3}$ at 1 bar to 8.94 kWh/kg$_{NH3}$ at 8 bar, showing the lowest demand at all pressures.

Breakdown by component (Fig. 3b–f) showed that the SOEC dominated energy consumption, followed by the evaporator, heaters, compressors, and the ASU unit. These values exclude heat integration, which is addressed in subsequent sections.

The specific energy consumption of SOEC and ASU decreased only slightly (~0.03%) when pressure increased from 1 to 8 bar, with marginally lower values in the sweep air-free system. These marginal changes resulted from minor deviations in global synthesis gas conversion in the HB reactor (Fig. S2 and SM).

The evaporator's specific energy demand decreased with pressurization in all configurations, primarily driven by the reduced enthalpy of vaporization from 40.7 kJ/mol at 1 bar to 36.9 kJ/mol at 8 bar. The value decreased from 1.44 kWh/kg$_{NH3}$ at 1 bar to 1.34 kWh/kg$_{NH3}$ at 8

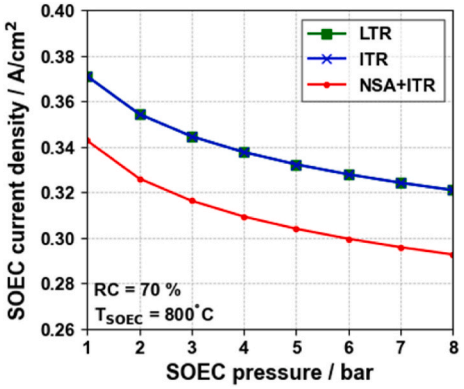

Fig. 2. SOEC current density at RC = 70% and 800 °C for LTR, ITR, and NSA + ITR changing with SOEC operating pressure from 1 to 8 bar.

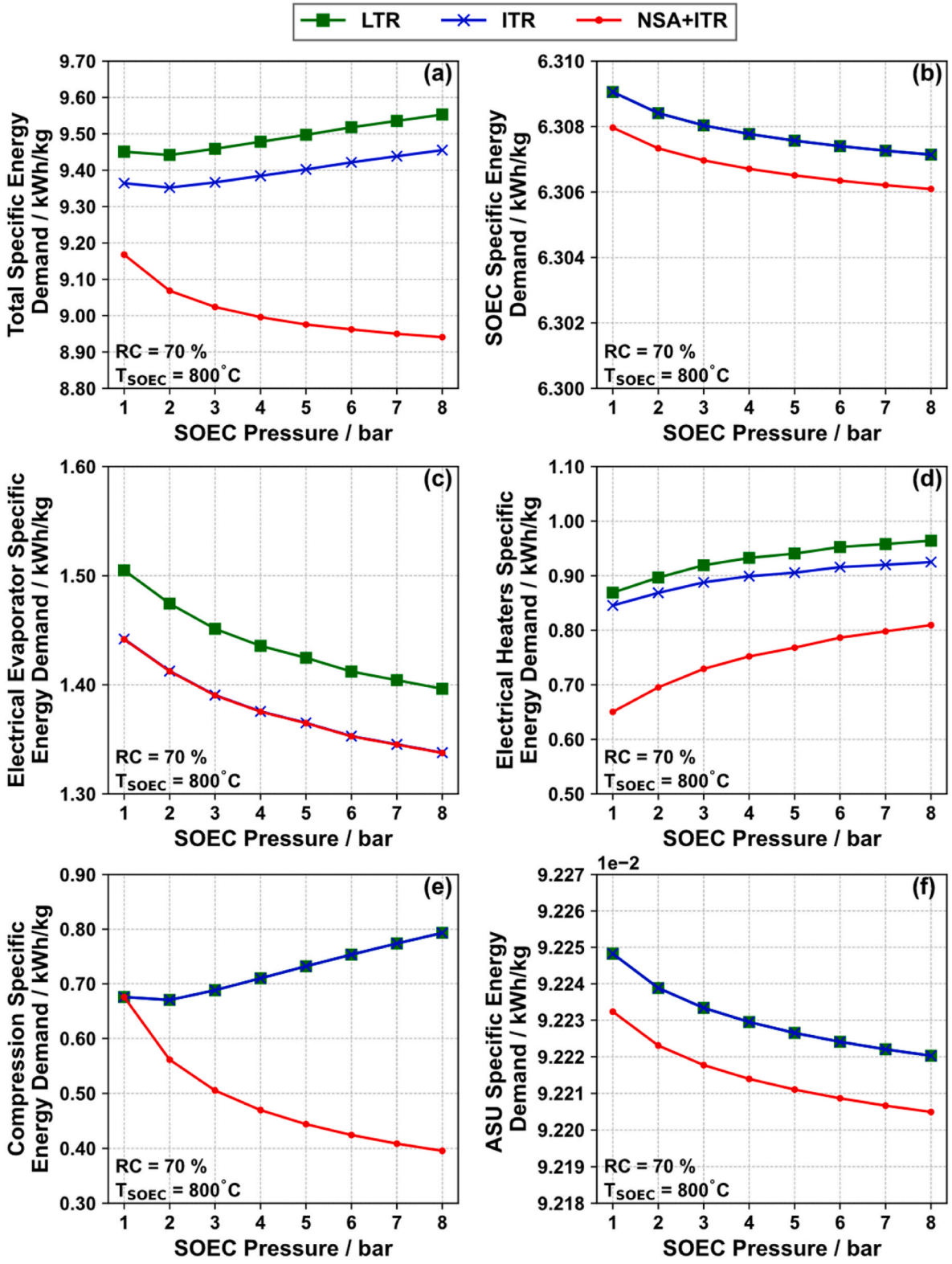

Fig. 3. Specific energy demand results for LTR, ITR and NSA + ITR routes with changing the SOEC pressure from 1 to 8 bar, RC = 70% and SOEC temperature of 800 °C. The specific energy demand is presented as: (a) total, (b) SOEC, (c) electrical evaporator, (d) electrical heaters, (e) compression/pump, and (f) ASU.

bar in the ITR, both with and without sweep air. LTR demands were higher, ranging from 1.50 kWh/kg_{NH3} (1 bar) to 1.40 kWh/kg_{NH3} (8 bar), due to condensation and liquid recirculation increasing water mass flow through the evaporator (e.g. 129.7 t/h to 135.3 t/h at 1 bar).

Electrical heater demand increased with pressure due to the higher boiling point of water, raising liquid water heating in LT-F1, which outweighed reduced steam heating in HT-F1 due to higher specific heat capacity of water than steam (Fig. S3 and SM) [9]. This increase in sensible heat consumption with pressure was higher than the discussed reduction of latent heat due to the reduced enthalpy of vaporization, leading to a net increase in power consumption for fuel gas heating including evaporation. NSA + ITR showed the lowest values (0.65–0.81

kWh/kg_{NH3}) due to no sweep air. The effect of heating sweep air up the SOEC operating temperature reflected in increased ITR demands of 0.20 kWh/kg_{NH3} at 1 bar and 0.11 kWh/kg_{NH3} at 8 bar. This difference decreased at higher pressures due to the reduced heating demand in HT-A1, as isentropic compression raises the stream's temperature during pressurization. In LTR, electrical heater demand was even slightly higher (0.02-0.04 kWh/kg_{NH3}) due to SOEC off-gas cooling to 25 °C before recirculation.

Specific compression energy demand (including compressors and pumps) gradually decreased from 0.68 kWh/kg_{NH3} at 1 bar to 0.40 kWh/kg_{NH3} at 8 bar in NSA + ITR, showing the advantage of liquid water pressurization. In contrast, LTR and ITR showed a minimum of 0.67 kWh/kg_{NH3} at 2 bar, subsequently increasing to 0.79 kWh/kg_{NH3} at 8 bar due to rising sweep air compression (Comp-A1, Fig. S4 in SM) overcompensating hydrogen downstream compression savings in (Comp-C1). Specific pumping energy was negligible ($\sim 5 \times 10^{-4}$ kWh/kg_{NH3}).

System LHV efficiencies (Fig. 4) inversely followed total specific energy demand (Fig. 3a). Perfect high-grade heat availability (PHA) LHV efficiencies, also shown in Fig. 4, assumed full coverage of evaporator and electrical heater demand by available excess heat. The values were inversely correlated with the specific compression energy (Fig. 3e).

NSA + ITR achieved the highest efficiencies, with PHA LHV increasing from 73.0% at 1 bar to 76.1% at 8 bar, showing a 3% point increase with pressurization due to reduced compressor power, in particular between 1 and 2 bar. NSA + ITR LHV efficiency increased from 56.4% at 1 bar to 57% at 2 bar, and 57.8% at 8 bar, driven by reduced heater demand low pressures and compression savings at high pressures.

ITR showed modest LHV efficiency gains (0.51-0.56%) compared to LTR, both peaking at 2 bar (55.3% and 54.7%). In contrast, no differences in PHA LHV efficiency were observed between them, with a maximum of 73.1% at 2 bar.

A detailed heat integration study is presented in subsection 3.3 to assess whether these savings yield actual performance improvements in a real heat integrated system, providing a foundation for an optimized system layout.

In summary, besides SOEC, the evaporator, heaters, and compressors significantly contribute to specific energy demand in SOEC-based PtA systems. The following section focuses specifical design aspects of the SOEC system by considering different recirculation strategies.

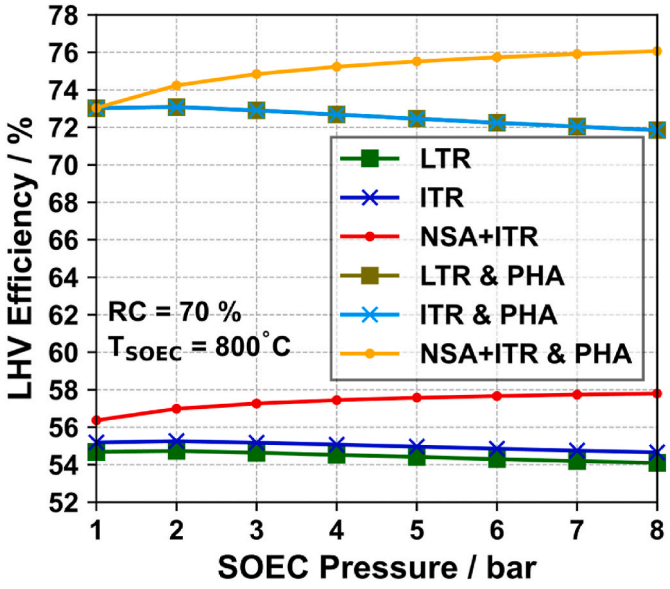

Fig. 4. System LHV efficiency and perfect high-grade heat availability LHV efficiency for LTR, ITR and NSA + ITR routes changing with SOEC operating pressure from 1 to 8 bar.

3.2. Influence of recirculation ratio on system performance

LTR and ITR strategies showed only minor efficiency differences in the previous subsection, partly due to the low recirculation ratio (RR) of 0.137 selected to ensure a minimum hydrogen content of 10% at the SOEC fuel inlet, thereby maintaining the Ni-based electrode in a reduced state. This subsection evaluates the effect of higher RRs on current density and system efficiency. Performance is assessed using LHV efficiency without heat integration (LHV), PHA LHV efficiency, and the HI LHV efficiency whereby partial heat integration is assumed and only the fuel and air trim heaters (HT-F1 and HT-A1) remain electrically heated.

For all configurations, the SOEC pressure was fixed at 2 bar, corresponding to peak LHV efficiency for sweep air systems. At a constant single-pass RC of 70%, RR was varied between 0.137, 0.416, 0.588, and 0.741, yielding global RC values of 73% (baseline), 80%, 85%, and 90%, respectively.

Increasing global RC reduced the isothermal SOEC current density (Fig. 5a) due to higher OCV from increased hydrogen inlet concentration according to the Nernst equation. For LTR and ITR, current density decreased from 0.35 A/cm^2 at 73% global RC to 0.27 A/cm^2 at 90%. NSA + ITR values were consistently 0.03 A/cm^2 lower at all operating points, consistent with trends observed in section 3.1.

At the system level, LHV efficiency exhibited different trends with increasing global RC for LTR and ITR (Fig. 5b and c). In ITR, LHV efficiency increased from 55.3% at 73% global RC to 56.6% at 90%, driven by a reduced heating demand, which decreased from 3.69 to 3.21 kWh/kg_{NH3}. This was primarily due to a lower electric evaporator energy demand (Fig. S5 and SM), as the recirculated stream bypassed the evaporator, reducing heating by 0.27 kWh/kg_{NH3}. Additional savings resulted from lower demand in the water pre-heater LT-F1 and reduced fuel gas trim heating in HT-F1 due to higher recirculation temperatures (265-318 °C). NSA + ITR exhibited the same LHV efficiency trend (Fig. 5d) as ITR, with a fairly constant increase of 1.8% points across all global RC values.

In contrast, LTR LHV efficiency decreased from 54.7% at 73% global RC to 52.2% at 90%. In this route, the recirculation occurred at 25 °C before flash FL1, resulting in a stream consisting mainly of liquid water and hydrogen gas. Increasing the RR increased the hydrogen content at the SOEC inlet, increasing Nernst voltage, while specific water flow through the evaporator and the associated heat demand remained nearly constant (Fig. S5). As a result, higher global RC offers no energetic benefit in LTR.

In contrast to the LHV efficiency, the PHA efficiency remained nearly constant for all global RC values, reaching 73.1% for LTR and ITR, and increasing from 74.2% to 74.3% for the NSA + ITR. Since evaporator and heater demands were assumed to be fully covered, this efficiency is not affected by the requirements in those components, therefore, it represents the highest efficiency that the defined systems could reach.

HI LHV efficiency, representing partial heat integration, lay between the LHV and PHA LHV efficiencies, and decreased with increasing global RC for all routes (Fig. 5). This decrease was mainly due to the larger recycle stream flow through the electrical trim heater HT-F1, increasing its heat demand (Fig. S5). LTR showed the lowest efficiencies, decreasing from 68.3% to 66.0%, while slightly higher values were observed for ITR, ranging from 68.4% to 67.6%. NSA + ITR consistently achieved the highest efficiencies, ranging from 71.1% to 70.1%.

The results show that the potential thermodynamic benefits of a higher RR depend on the specific recirculation strategy and the available heat for integration, particularly for water evaporation. Therefore, a detailed heat integration study was conducted in the following.

3.3. Heat integration

The actual LHV efficiency of a real system depends on the level of

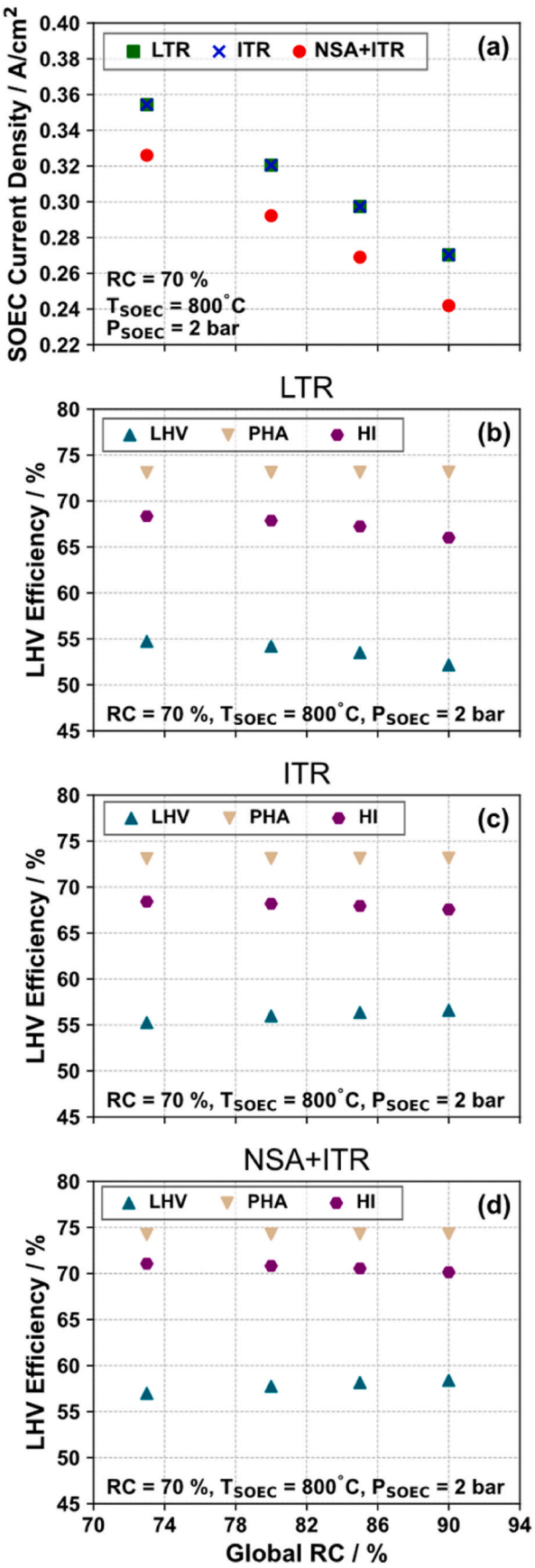

Fig. 5. (a) Current density, and LHV, PHA and HI efficiencies for (b) LTR, (c) ITR, and (d) NSA + ITR with SOEC operating at 800 °C, 2 bar and RC = 70% and global RC of 73%, 80%, 85% and 90%.

heat integration and the design of the HEN, and may differ significantly from the previous assumptions. In particular, it is unclear whether sufficient excess heat is available for pure thermal steam generation. Therefore, a detailed heat integration study was conducted for all three system configurations at SOEC pressures of 1, 2 and 8 bar, and 73% global RC, yielding an optimized HEN for each route. Hot and cold stream matching varied slightly with pressure, and the generalized PFD is depicted in Fig. S6 in SM.

Fig. 6 summarizes the specific energy demand of SOEC, ASU, compression/pumping and electrical heating, and the LHV efficiency of the proposed system layouts. SOEC, ASU, and compression/pump specific energy demand match Fig. 3, since they were unaffected by heat integration. In all cases, except for NSA + ITR at 8 bar, the water preheater LT-F1, evaporator EV-F1, and HB loop trim heater HE-HB1 heating demands were fully covered by excess off-gas heat. However, trim heaters on SOEC air and the fuel side, HT-A1 and HT-F1, still required electrical power since no high-temperature heat was available ('Electrical heating' in Fig. 6). The NSA + ITR system showed a ~0.2 kWh/kg_{NH3} lower specific heater demand than ITR and LTR due to the absence of an oxygen side trim heater, increasing LHV efficiency increase by 2% at atmospheric pressure.

Fig. 7a shows the sources of heat for steam generation, including internal SOEC fuel/air off-gas heat, compression intercooler (CO-C1 and Multi-Comp), ammonia synthesis heat, and electrical heating.

Interestingly, across all conditions a total of 29.9-62.3% of steam demand could be supplied via economizers during internal SOEC heat recovery. However, only 27% of this steam was effectively converted to hydrogen, reflecting the 73% global RC. Compression intercoolers contributed 30.9-33.6% at atmospheric pressure, while the HB reaction heat only supplied 35-36.6%. At higher pressures, internal steam generation became more challenging due to higher water boiling points of up to 170 °C, which requires a higher-grade heat source. This reduced contribution of the intercoolers to water evaporation and increased the share of the waste heat stream for water preheating (Fig. 7b). Simultaneously, the HB reaction heat contribution to water evaporation increased to 37.8-39.4% at 8 bar.

In NSA + ITR at 8 bar, oxygen-side off-gas had reduced mass flow and thermal capacity, which restricted available high-temperature heat. Consequently, it was the only system that required additional electrical input to generate 8.1% steam. Pressurized NSA + ITR systems even utilized the low-temperature CO-HB2 heat ('from HB reaction heat' in Fig. 7b), not recovered in other systems.

One strategy to reduce the deficit is to increase the RR/global RC. Increasing the global RC from 73% to 90% decreased evaporator energy demand and eliminated the need for electrical steam generation, yielding the highest system LHV efficiency of 72.1% and a total specific energy demand of 7.17 kWh/kg_{NH3} comparable to the 7.3-7.4 kWh/kg_{NH3} from previous studies [12,30]. However, this came with a low current density of 0.21 A/cm^2, highlighting the trade-off between production rate and efficiency. While the 0.2 percentage point LHV efficiency gain over NSA + ITR at 8 bar appears modest, higher pressures may yield larger efficiency improvements as thermal water evaporation from internal heat integration sources becomes increasingly difficult.

More broadly, operating pressure had a positive effect on NSA + ITR efficiency, with LHV efficiency increasing from 69.9% at 1 bar to 71.8 % at 8 bar. In contrast, at 2 bar, maximum LHV efficiencies were only 68.3 % for LTR and 68.4 % for ITR, highlighting the potential of pressurized SOECs operated with pure oxygen. Reflecting this trend, industrial manufacturers are increasingly developing pressurized SOEC technologies that eliminate air compression. For example, Sunfire (Germany) offers 10 MW SOEC modules producing pure oxygen without sweep air [24], while stacks from Topsoe A/S (Denmark) tolerate differential pressure between the oxygen and fuel sides [31]. Pressures vessels are typically used to avoid differential pressures between fuel side and environment, which may increase CAPEX. Moreover, safety issues coming from potential hydrogen leakages into the pressure vessel need

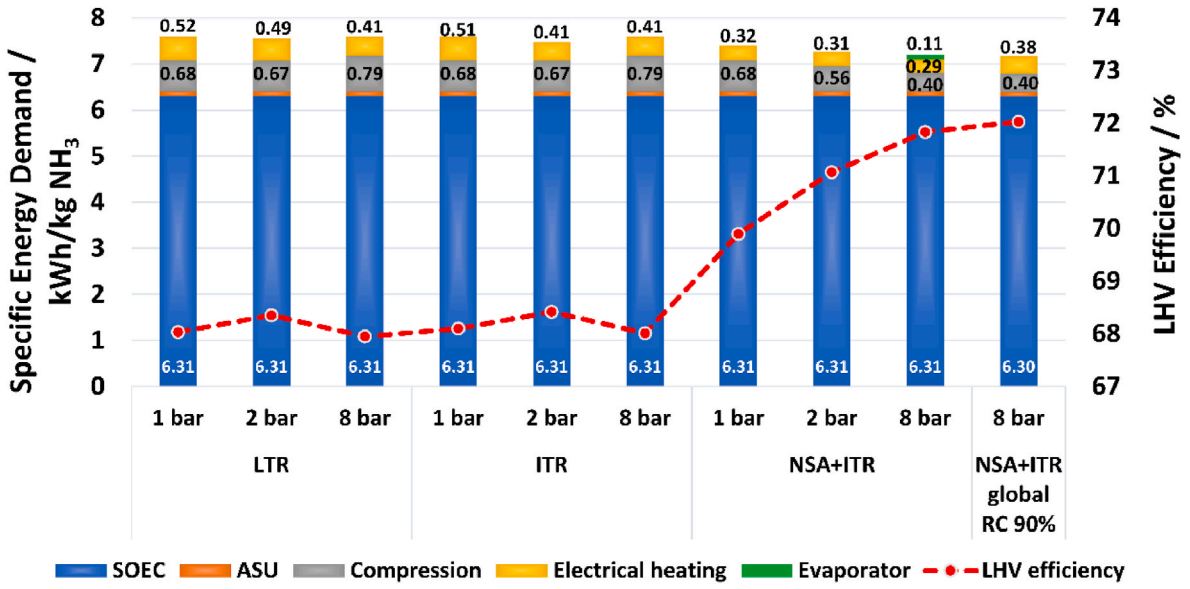

Fig. 6. Specific energy demand distribution and LHV efficiency for LTR, ITR, and NSA + ITR systems at SOEC pressures of 1, 2 and 8 bar, plus the NSA + ITR at global RC of 90% and SOEC pressure of 8 bar. For all the cases the ASU specific energy demand is 0.09 kWh/kg_{NH3} (the values are not presented in the figure).

to be carefully avoided.

The calculated system efficiencies in the present study align with literature values of 70-74% [12,30]. Heat losses from the HB reactor were neglected, which could decrease specific energy consumption. A purge gas ratio of 2% was assumed, a common value in conventional HB processes, but SOEC-based PtA processes could use lower ratios due to the absence of inert gases such as argon in the hydrogen supply. The results exceed the 56-57% efficiencies of PtA systems based on alkaline and polymer exchange membrane (PEM) electrolysis by more than 15 percentage points [12,32], and are higher than the experimentally observed 62-65% efficiency of optimized HB plants (specific energy demand of 7.6-8.8 kWh/kg_{NH3}) based on methane reforming [33].

3.4. Part-load study

While the previous section has identified the most efficient system configuration under full-load conditions, a part-load study was also conducted since fluctuating RES supply likely require dynamic operation and part-load operation of PtX systems. The established HB process, with multiple high-pressure compressors and extensive heat integration, is inherently difficult to operate dynamically [33]. Large-scale plants generally maintain operation between 65% and 100% of nominal load to meet minimum flow requirements and avoid overheating [34,35]. To reduce minimum load limits, strategies such as modifying RRs or redesigning heat exchangers have been proposed [36,37], with minimum loads as low as 10% suggested [35,38].

Dynamic SOEC operation was long considered challenging due to the mechanical susceptibility of ceramics-based stacks towards thermal gradients. However, recent studies demonstrated higher dynamic stack stability than previously assumed [39,40], and novel operating strategies such pulse-width modulation (PWM) have been suggested [41,42]. Given the modular design of SOEC plants, a modular on/off switching strategy is more likely than direct load-following of all stacks, with some operating near full load while others remain in hot standby [43].

In this study, a modular system at 2 bar with ITR was assumed, operating at 60% and 10% of the nominal load, corresponding to the current and projected minimum HB reactor loads. Hot standby requires significant electricity for heaters and air compressors.

Table 1 shows heating duties, work demand of the different system components and the entire system, and system efficiencies for hot standby, 10%, 60% and 100% load. Fig. 8 shows the specific energy demand distribution. SOEC and ASU energy consumption scaled proportionally with load, while an increasing number of modules in hot standby increased compressor and electrical heater consumption. This led to an increase in specific electrical heating duty from 0.48 kWh/kg_{NH3} at 100% load to 3.35 kWh/kg_{NH3} at 10% load, and a specific work demand increase from 7.07 kWh/kg_{NH3} at 100% load to 8.16 kWh/kg_{NH3} at 10% load. Consequently, total specific electrical demand increased hyperbolically from 7.55 kWh/kg_{NH3} at 100% load to 7.85 kWh/kg_{NH3} at 60% load and 11.51 kWh/kg_{NH3} at 10% load. A similar behavior with a slightly lower value of 10.56 kWh/kg_{NH3} (~38 GJ/t_{NH3}) has been reported at 10% part-load in a previous study [30]. The increase in specific energy consumption resulted in a system efficiency decrease of ~45% at 10% load, notably lower than reported values of 56-57% for low-temperature electrolysis-based PtA systems at nominal load, which avoid air compression and large heat losses.

The results show that heat losses from SOEC modules in hot standby significantly decrease system efficiencies at low loads. The increase in operating expenditure (OPEX) due to higher specific energy consumption may justify the use of batteries to buffer short-term periods of high electricity prices. During extended periods of limited RES availability, it may become energetically and economically advantageous to lower hot-standby temperatures, switch to cold standby, or exploit reversible SOC operation, allowing some modules to generating electricity to sustain others.

Although heat integration results across the entire 10–100% load range show consistent hot and cold stream matching, practical heat exchanger design is challenging. Heat exchanger sizing is typically governed by full-load operation, while reduced heat-transfer coefficients and pressure-drop variations at part-load can impair performance and controllability. Fixed configurations cannot adapt dynamically, making careful exchanger sizing and flexibility essential for robust operation under variable load conditions.

The presented part-load results were based on specific assumptions. SOEC, ASU and HB loop were operated at the same part-load at all operating points, assuming no gas storage. In practice, SOEC-based PtA systems are anticipated to use gas storage tanks to harmonize the different dynamics of SOEC, ASU and ammonia synthesis, and to prevent over-sizing the synthesis reactor for SOEC peak production [14]. Accordingly, a continuous supply of process heat for SOEC steam generation must be ensured, particularly during synthesis reactor downtime, likely requiring advanced heat management systems, and

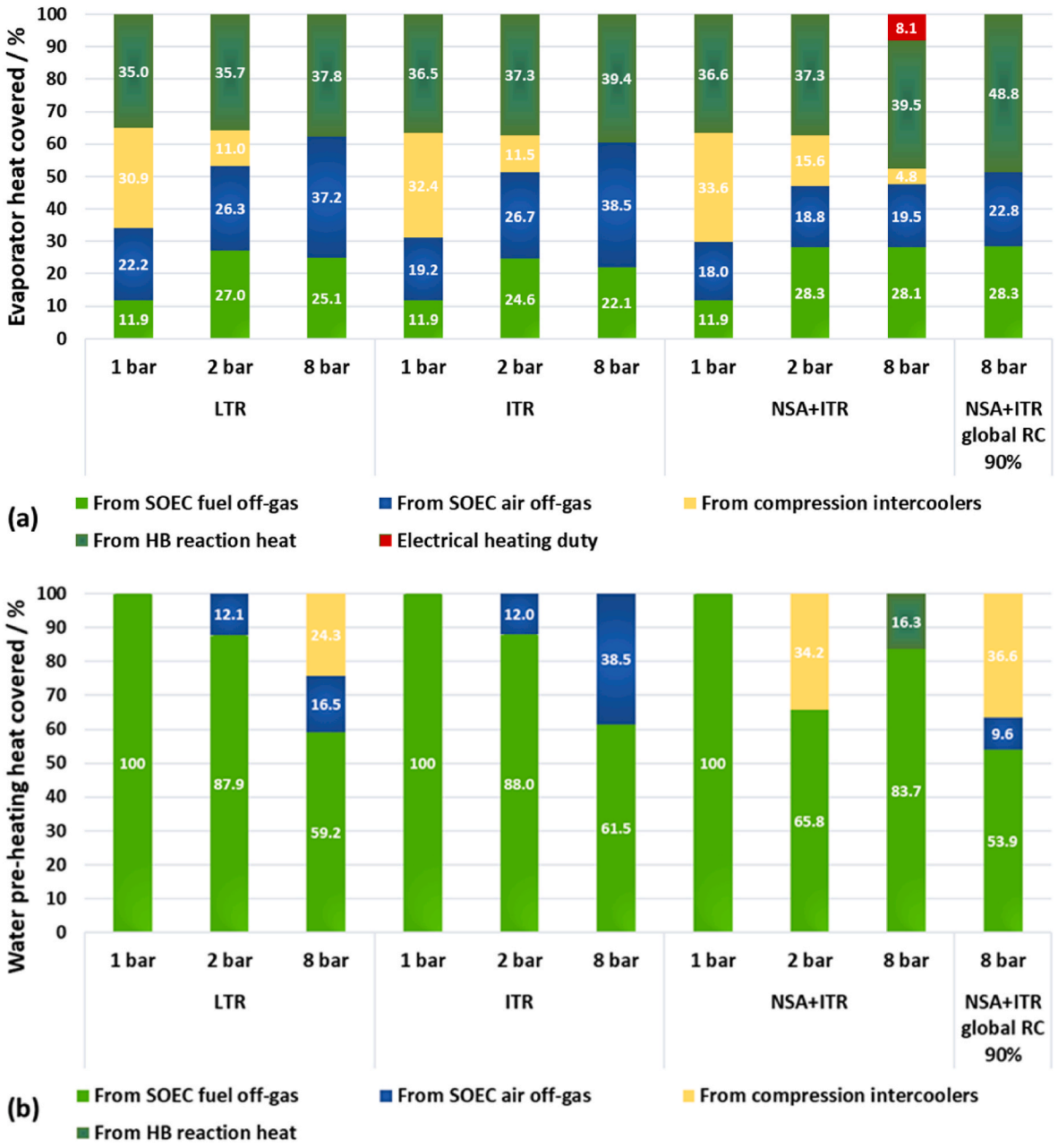

Fig. 7. (a) Evaporator heat demand percentage covered by SOEC fuel/air off-gases, compression intercoolers, HB reaction heat and extra heating duty, and (b) water pre-heating (LT-F1) heat demand percentage covered SOEC fuel/air off-gases, compression intercoolers, HB reaction heat, for LTR, ITR, NSA + ITR systems at 1, 2 and 8 bar, and the NSA + ITR system with global RC = 90% and 8 bar. Absolute values are shown in Fig. 3c.

electrical steam generation. However, SOEC-based PtA systems with gas storage were beyond the scope of this study.

The assumption of the quasi-linear behavior of compressors and the ASU is a simplification. In industry, hydrogen compression often relies on membrane compressors or dry running reciprocating piston compressors, which can operate down to 20% load [21,44]. In contrast, large-scale HB plants typically use centrifugal compressors due to their high reliability and ability to handle large flow rates, which are less flexible and usually limited to 50-60% minimum load [21]. Lower part-load operation may be achievable via kickback-operation, as recently investigated for SOEC-based PtA systems [30]. ASUs typically operate between 60 and 100% load, also constrained by centrifugal compressors [45]. In addition, compression efficiency typically decreases at off-design points, an effect not considered here.

Despite these simplifications, the results reveal important load-dependent trends. More detailed part-load studies incorporating load-dependent system component behavior and storage solutions such as gas tanks or batteries, are needed to better optimize flexibility and efficiency.

4. Conclusions

This work demonstrates the high efficiency potential of SOEC-based PtA systems, particularly under pressurized operation without sweep air. Using an experimentally validated isothermal ESC model, the effects of system pressure, recirculation strategies, and heat integration on efficiency were evaluated. The sweep air-free configuration at 8 bar achieved the highest efficiencies, up to 72%, primarily due to reduced compression demand. Sweep air configurations allow for greater heat recovery via larger off-gas mass flow, but introduce additional

Table 1
Energy balance and efficiency results for all load and hot-standby scenario combinations.

Parameter	Details	Load %/hot standby %			
		0/100	10/90	60/40	100/0
Product flow	NH_3 ton/h	-	5.50	32.95	54.88
Electrical heating	Electrical heating power MW	17.49	18.43	23.20	26.49
	Specific heating kWh/kg	-	3.35	0.70	0.48
Power demand	SOEC MW	-	34.65	207.72	346.20
	Specific SOEC kWh/kg	-	6.297	6.303	6.308
	Comp/pump MW	6.72	9.73	24.75	36.78
	Specific comp/pump kWh/kg	-	1.77	0.75	0.67
	ASU MW	-	0.51	3.04	5.06
	Specific ASU kWh/kg	-	0.09	0.09	0.09
	Total power MW	6.72	44.85	235.51	388.04
	Total specific energy kWh/kg	-	8.16	7.15	7.07
Total electrical demand	Total MW	24.21	63.28	258.71	414.53
	Total specific kWh/kg	-	11.51	7.85	7.55
Efficiency	LHV efficiency %	-	44.89	65.83	68.42

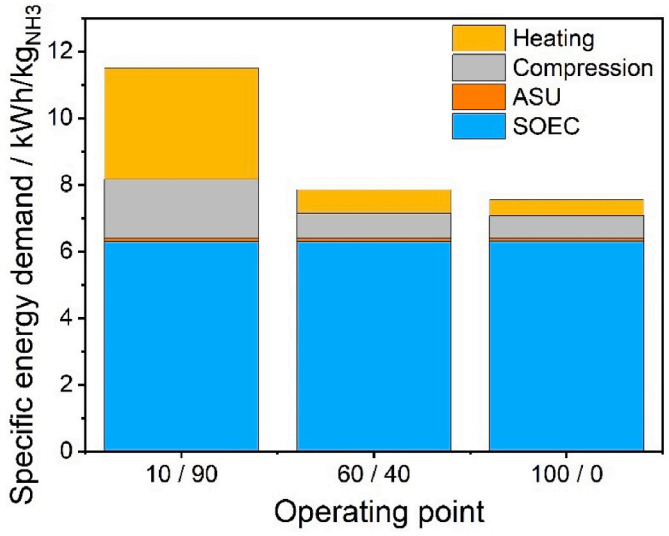

Fig. 8. Specific energy demand distribution of the modular system with ITR at 2 bar and partial-load scenarios of 10%, 60% and 100% of the nominal load including heat integration with an optimized HEN. Exact values are listed in Table 1.

compression penalties, lowering efficiencies (~69%). Up to 62% of SOEC steam demand can be met through thermal recovery from SOEC fuel and oxygen side off-gas heat. Higher single-pass RCs than the assumed 70% could even increase this value. In most cases, remaining steam demand was met using waste heat from the downstream HB loop, with no efficiency differences between LTR and ITR observed. High-pressure operation without sweep air can lead to incomplete thermal steam generation due to lower off-gas enthalpy and higher boiling temperatures. These limitations can be mitigated by increasing the global recirculation ratio in ITR configurations, reducing evaporator load and avoiding electrical steam generation. LTR configurations cannot use this strategy effectively, as higher recirculation only marginally lowers evaporator energy. Overall, pressurized SOEC systems with pure oxygen can outperform low-temperature electrolysis PtA pathways by over 15 percentage points. Part-load operation decreases system efficiency down to 45% at 10% load due to the electrical module heating in hot standby. As a result, prolonged periods of modules in hot standby should be avoided.

CRediT authorship contribution statement

Daruska Miric-Fuentes: Writing – original draft, Software, Methodology, Investigation, Formal analysis, Data curation. **Matthias Riegraf:** Writing – original draft, Visualization, Supervision, Investigation, Formal analysis, Conceptualization. **Faisal Sedeqi:** Writing – original draft, Software, Methodology, Investigation, Formal analysis, Data curation. **Srikanth Santhanam:** Writing – review & editing, Formal analysis, Conceptualization. **Marc P. Heddrich:** Writing – review & editing, Resources, Funding acquisition. **S. Asif Ansar:** Resources, Supervision.

Declaration of competing interest

The authors declare the following financial interests/personal relationships which may be considered as potential competing interests: All authors reports financial support was provided by Shell Global Solutions International BV. If there are other authors, they declare that they have no known competing financial interests or personal relationships that could have appeared to influence the work reported in this paper.

Acknowledgments

This work was financially supported by Shell Global Solutions International B.V. within the project HTeNH3.

Appendix A. Supplementary data

Supplementary data to this article can be found online at https://doi.org/10.1016/j.renene.2026.125528.

References

[1] W.I.F. David, et al., "2023 roadmap on ammonia as a carbon-free fuel", J. Phys.: Energy 6 (2) (2024/02/06) 021501, https://doi.org/10.1088/2515-7655/ad0a3a, 2024.
[2] M. Appl, Ammonia, 2. production processes, in: Ullmann's Encyclopedia of Industrial Chemistry, Wiley-VCH, Weinheim, 2012.
[3] Bloom Energy. https://www.bloomenergy.com/wp-content/uploads/bloom-energy-electrolyzer-datasheet-december-2023.pdf (accessed December 2025).
[4] C. Wulf, P. Zapp, A. Schreiber, Review of power-to-X demonstration projects in Europe, Front. Energy Res. 8 (2020) 191, https://doi.org/10.3389/fenrg.2020.00191.
[5] S.H. Jensen, C. Graves, M. Chen, J.B. Hansen, X. Sun, Characterization of a planar solid oxide cell stack operated at elevated pressure, J. Electrochem. Soc. 163 (14) (2016/11/19) F1596, https://doi.org/10.1149/2.1171614jes, 2016.
[6] O. Posdziech, K. Schwarze, J. Brabandt, Efficient hydrogen production for industry and electricity storage via high-temperature electrolysis, Int. J. Hydrogen Energy 44 (35) (2019/07/19) 19089–19101, https://doi.org/10.1016/j.ijhydene.2018.05.169, 2019.
[7] J.B. Hansen, N. Christiansen, J.U. Nielsen, Production of sustainable fuels by means of solid oxide electrolysis, ECS Trans. 35 (1) (2011/04/25) 2941, https://doi.org/10.1149/1.3570293, 2011.
[8] S. Gupta, M. Riegraf, R. Costa, M.P. Heddrich, K.A. Friedrich, Solid oxide electrolysis cell-based syngas production and tailoring: a comparative assessment of coelectrolysis, separate steam, CO2 electrolysis, and steam electrolysis, Ind. Eng. Chem. Res. (2024/05/07), https://doi.org/10.1021/acs.iecr.3c03674, 2024.
[9] D. Miric-Fuentes, F. Sedeqi, M. Riegraf, S. Santhanam, M. Heddrich, S.A. Ansar, The effect of pressure and temperature on exergy efficiency in Power-to-Methane: a comparison of steam and Co-Electrolysis, Energy Convers. Manag. X 28 (2025) 101394.
[10] M. Henke, S. Hillius, M. Riedel, J. Kallo, K.A. Friedrich, Gas recirculation at the hydrogen electrode of solid oxide fuel cell and solid oxide electrolysis cell systems, Fuel Cells 16 (5) (2016) 584–590.
[11] M. Frank, R. Deja, R. Peters, L. Blum, D. Stolten, Bypassing renewable variability with a reversible solid oxide cell plant, Appl. Energy 217 (2018) 101–112.
[12] H. Nami, P.V. Hendriksen, H.L. Frandsen, Green ammonia production using current and emerging electrolysis technologies, Renew. Sustain. Energy Rev. 199 (2024/07/01) 114517, https://doi.org/10.1016/j.rser.2024.114517, 2024.

[13] H. Zhang, L. Wang, J. Van herle, F. Maréchal, U. Desideri, Techno-economic comparison of green ammonia production processes, Appl. Energy 259 (2020/02/01) 114135, https://doi.org/10.1016/j.apenergy.2019.114135, 2020.
[14] A. Tremel, Electricity-Based Fuels, Springer International Publishing, Cham, Switzerland, 2018.
[15] D. Frattini, G. Cinti, G. Bidini, U. Desideri, R. Cioffi, E. Jannelli, A system approach in energy evaluation of different renewable energies sources integration in ammonia production plants, Renew. Energy 99 (2016/12/01) 472–482, https://doi.org/10.1016/j.renene.2016.07.040, 2016.
[16] A. Lima, J. Torrubia, C. Torres, A. Valero, A. Valero, Dynamic small-scale green ammonia non-renewable and renewable exergy costs up to 2050: short and long-term projections under IEA energy transition scenarios, Renew. Energy 256 (2026/01/01) 123891, https://doi.org/10.1016/j.renene.2025.123891, 2026.
[17] G. Barreto, M. Romero, J. González-Aguilar, A. Giaconia, M. Testi, Design point, part load and annual performance analysis of a 100 kW SOEC system integrating a solar steamer under electrolyser operational constraints, Renew. Energy 256 (2026/01/01) 124340, https://doi.org/10.1016/j.renene.2025.124340, 2026.
[18] M. Amin, et al., Issues and challenges in hydrogen separation technologies, Energy Rep. 9 (2023) 894–911, https://doi.org/10.1016/j.egyr.2022.12.014.
[19] A. Attari Moghaddam and U. Krewer, "Poisoning of ammonia synthesis catalyst considering off-design feed compositions," Catalysts, vol. 10, no. 11, doi: 10.3390/catal10111225.
[20] J. Ikäheimo, J. Kiviluoma, R. Weiss, H. Holttinen, Power-to-ammonia in future North European 100 % renewable power and heat system, Int. J. Hydrogen Energy 43 (36) (2018) 17295–17308, https://doi.org/10.1016/j.ijhydene.2018.06.121.
[21] P. Gallick, G. Phillippi, B.F. Williams, What's correct for my Application-A centrifugal or reciprocating compressor?. Proceedings of the 35th Turbomachinery Symposium, 2006, pp. 113–120.
[22] H. Zhang, L. Wang, J. Van herle, F. Maréchal, U. Desideri, Techno-economic comparison of green ammonia production processes, Appl. Energy 259 (2020), https://doi.org/10.1016/j.apenergy.2019.114135.
[23] J.C. Morud, S. Skogestad, Analysis of instability in an industrial ammonia reactor, AIChE J. 44 (4) (1998) 888–895, https://doi.org/10.1002/aic.690440414.
[24] S.E. Sunfire. https://backend.sunfire.de/wp-content/uploads/2024/10/Sunfire_Fact-Sheet_SOEC_EN_digital.pdf (accessed December 2025).
[25] A. Mai, et al., Recent advances in Power-to-X and SOEC activities at Topsoe, in: 16th European SOFC & SOE Forum, Lucerne, Switzerland, 2024.
[26] R.K. Sinnott, Butterworth -Heinemann (Eds.), Chemical Engineering Design, fourth ed., 2005. Oxford.
[27] T. Bui, D. Lee, K.Y. Ahn, Y.S. Kim, Techno-economic analysis of high-power solid oxide electrolysis cell system, Energy Convers. Manag. 278 (2023) 116704, https://doi.org/10.1016/j.enconman.2023.116704, 2023/02/15.
[28] M. Lang, S. Raab, M.S. Lemcke, C. Bohn, M. Pysik, Long-Term behavior of a solid oxide electrolyzer (SOEC) stack, Fuel Cells 20 (6) (2020) 690–700.
[29] M. Riegraf, et al., Electrochemical analysis of an electrolyte-supported solid oxide cell-based MK35x stack during long-term electrolysis operation, J. Electrochem. Soc. 171 (2024) 054504, https://doi.org/10.1149/1945-7111/ad417f.
[30] M. Schiedeck, R. Nogueira Nakashima, H.L. Frandsen, Heat integration and part-load performance of an SOEC-coupled Haber–Bosch process, Int. J. Hydrogen Energy 116 (2025/04/04) 242–256, https://doi.org/10.1016/j.ijhydene.2025.02.335, 2025.
[31] T. Heiredal-Clausen, et al., Topsoe stack platform for upscaling and commercialization of SOEC in Power-to-X, in: 16th European SOFC & SOE Forum, Lucerne, Switzerland, 2024.
[32] S. Richard, et al., Power-to-ammonia synthesis process with membrane reactors: Techno- economic study, Int. J. Hydrogen Energy 73 (2024/07/04/2024) 462–474, https://doi.org/10.1016/j.ijhydene.2024.06.041.
[33] C. Smith, A.K. Hill, L. Torrente-Murciano, Current and future role of Haber–Bosch ammonia in a carbon-free energy landscape, Energy Environ. Sci. 13 (2) (2020) 331–344, https://doi.org/10.1039/C9EE02873K, 10.1039/C9EE02873K.
[34] J. Fuhrmann, M. Hülsebrock, U. Krewer, Energy storage based on electrochemical conversion of ammonia, Transition to Renewable Energy Systems (2013) 691–706.
[35] R. Ostuni, F. Zardi, Method for load regulation of an ammonia plant, US Patent Application 13 (626) (2012) 25, 316.
[36] M. Rizzi, Control of an Ammonia Synthesis Loop at Partial Load, vol. 148, U.S. Patent Application, 2023. No. 17/770.
[37] C.H. Speth, M. Hultqvist, P.A. Han, Method for the Control of Pressure in a Loop for the Preparation of Ammonia or Methanol, U.S. Patent Application, 2023, p. 833. No. 17/918.
[38] K. Verleysen, A. Parente, F. Contino, How sensitive is a dynamic ammonia synthesis process? Global sensitivity analysis of a dynamic Haber-Bosch process (for flexible seasonal energy storage), Energy 232 (2021/10/01) 121016, https://doi.org/10.1016/j.energy.2021.121016, 2021.
[39] H. Liu, J. Høgh, P. Blennow, X. Sun, Y. Zong, M. Chen, Assessing fluctuating wind to hydrogen production via long-term testing of solid oxide electrolysis stacks, Appl. Energy 361 (2024/05/01) 122938, https://doi.org/10.1016/j.apenergy.2024.122938, 2024.
[40] M. Riegraf, et al., Reversible long-term operation of a MK35x electrolyte-supported solid oxide cell-based stack, J. Electrochem. Soc. 171 (10) (2024/10/07) 104505, https://doi.org/10.1149/1945-7111/ad8036, 2024.
[41] N. Kane, et al., Accelerated stress testing of standard solid oxide electrolysis cells, ECS Trans. 111 (6) (2023) 2139.
[42] O. Posdziech, T. Strohbach, R. Blumentritt, K. Schwarze, C. Greß, Solid oxide cell (soc) operating method, European Patent Patent 3956497A1 (2022).
[43] M. Tomberg, M.P. Heddrich, S.A. Ansar, K.A. Friedrich, Operation strategies for a flexible megawatt scale electrolysis system for synthesis gas and hydrogen production with direct air capture of carbon dioxide, Sustain. Energy Fuels (2023), https://doi.org/10.1039/D2SE01473D, 10.1039/D2SE01473D.
[44] A. Peschel, Industrial perspective on hydrogen purification, compression, storage, and distribution, Fuel cells 20 (4) (2020) 385–393.
[45] S. Mucci, A. Mitsos, D. Bongartz, Power-to-X processes based on PEM water electrolyzers: a review of process integration and flexible operation, Comput. Chem. Eng. 175 (2023) 108260.